chemosensors

Article

Influence of Positive Ion (Al^{3+}, Sn^{4+}, and Sb^{5+}) Doping on the Basic Resistance and Sensing Performances of ZnO Nanoparticles Based Gas Sensors

Peng Zhang, Shuang Cao, Ning Sui, Yifeng Xu, Tingting Zhou *, Yuan He * and Tong Zhang

State Key Laboratory of Integrated Optoelectronics, College of Electronic Science and Engineering, Jilin University, Changchun 130012, China
* Correspondence: zhoutt@jlu.edu.cn (T.Z.); heyuan@jlu.edu.cn (Y.H.)

Abstract: Despite potential advantages of metal oxide semiconductors (MOSs)-based gas sensors, the limitation of very high baseline resistance is still unsatisfactory for practical application. By means of element doping, the performance of metal oxide materials used as gas sensors can be optimized. Herein, different cations (Al^{3+}, Sn^{4+}, and Sb^{5+}) doped ZnO nanoparticles were synthesized and used as the acetone sensing materials. Results show that the resistance of sensors based on Sn^{4+} doped ZnO was significantly reduced (from 5.18 to 0.28 MΩ) at 270 °C without sacrificing the acetone sensing responses. In addition, the gas sensor also exhibited the fast response/recovery time (1/10 s) and great long-term stability. The electron compensation and improved adsorbing oxygen ability for the Sn^{4+} doped ZnO nanoparticles contributed to the relatively low resistance and enhanced acetone sensing performances.

Keywords: ZnO nanoparticles; doping; gas sensors; acetone; low original resistance; electron compensation

Citation: Zhang, P.; Cao, S.; Sui, N.; Xu, Y.; Zhou, T.; He, Y.; Zhang, T. Influence of Positive Ion (Al^{3+}, Sn^{4+}, and Sb^{5+}) Doping on the Basic Resistance and Sensing Performances of ZnO Nanoparticles Based Gas Sensors. *Chemosensors* **2022**, *10*, 364. https://doi.org/10.3390/chemosensors10090364

Academic Editor: Boris Lakard

Received: 5 August 2022
Accepted: 6 September 2022
Published: 10 September 2022

1. Introduction

The exploration of high-performance gas sensors is particularly critical for the purpose of environmental monitoring and toxic analyte detecting [1,2]. Metal oxide semiconductors (MOSs)-based gas sensors possess unique advantages including high sensitivity, fast response/recovery time, convenient operation and portability [3–7]. Significant achievements have been attained in developing highly sensitive gas sensors based on MOSs with delicate morphology and complex components. Nevertheless, a major obstacle is the excessive increase in original resistance accompanied by the high response even at the higher operation temperature [8–13]. Thus, it is necessary to fabricate the gas sensors with both relatively low/measurable initial resistance and high response considering the circuit design in practical application.

Doping specific extrinsic metal elements has been regarded as a promising strategy to tailor the electronic/structural properties for semiconductors. Numerous studies have proven that the gas sensing property is closely related to the added dopant in the matrix. For example, Li et al. prepared 2 mol% Ru-doped SnO_2 nanotubes by using electrospinning technology [14]. The highest response can reach 340 toward 100 ppm of ethanol at 200 °C (original resistance: 780 KΩ). Shen et al. synthesized the 2 wt% Pd-doped SnO_2 nanowires by thermal evaporation of tin grains [15]. The 2 wt% Pd-doped SnO_2 nanowires show a high response (R_a/R_g = 253) to 1000 ppm of H_2 (original resistance: 450 MΩ). Park et al. developed 0.001 wt% Pt and 8 mol% Ga co-doped ZnO materials, which exhibited a considerably high response (R_a/R_g = 26.2) to 5 ppm of C_2H_2 (original resistance: 105 MΩ) [16]. High-resistance gas sensors will cause problems, such as the unstable signal interfered with by the environment and high-power consumption. It is still difficult to achieve both aforementioned goals (measurable initial resistance and high response) at the

same time. Thus, selecting and optimizing dopants rationally is particularly important, and is a factor to consider results from: (1) dopant cationic radius: the similar cationic radius of different metallic cations can easily be substituted in the MOS lattice to control the defect chemistry [17]; (2) dopant valence stats: the metal cation dopants with high valence stats can increase the carrier density to reduce the original resistance [18,19]; and (3) doping concentration: the concentration of additives should be less than the limiting solubility without forming clusters at the MOS grain surface [11,20,21].

Taking all considerations into account, high-valence-cation doping to ZnO was employed to decrease the basic resistance of gas sensors. Specifically, Al^{3+}, Sn^{4+}, and Sb^{5+} were selected as dopants. In order to optimize doping concentrations, different mole ratios of Al^{3+}, Sn^{4+}, and Sb^{5+} doping to ZnO were studied. Sensing results show that the sensors based on 0.5 mol% Sn doped ZnO exhibit relatively low basic resistance, high response, and fast response/recovery time.

2. Materials and Methods

2.1. Materials

Zinc acetate dihydrate ($Zn(CH_3COO)_2{\cdot}2H_2O$, 99.0%), aluminum chloride ($AlCl_3$, 99.0%), tin chloride pentahydrate ($SnCl_4{\cdot}5H_2O$, 99.0%), antimony trichloride ($SbCl_3$, 99.0%), and ammonia solution ($NH_3{\cdot}H_2O$, 25–28%) were of analytical grade and purchased from Shanghai Chemical Corp, China.

2.2. Synthesis Process

2.2.1. Synthesis of Sn Doped ZnO NPs

First, 1 g of Zn $(CH_3COO)_2{\cdot}2H_2O$ was dissolved in 20 mL of deionized water. Different amounts (0.5 mol%, 1 mol%, and 5 mol%) of $SnCl_4{\cdot}5H_2O$ were added into the solution and stirred with a magnetic stirrer at room temperature for 30 min. Then, ammonia solution (volume ratio, ammonia: deionized water = 1:4) was added dropwise to adjust the pH to 7~8. After stirring for 4 h, the solution turned into a white gel and then standing for 24 h. The precipitate was collected and washed several times with ethanol until the supernatant stopped reacting with silver nitrate solution to form precipitation. Finally, the product was calcined in air at 500 °C for 2 h to obtain the sample. Sn0.5-ZnO, Sn1-ZnO, and Sn5-ZnO correspond to 0.5 mol%, 1 mol%, and 5 mol% of Sn doped ZnO, respectively.

2.2.2. Synthesis of Al Doped ZnO NPs and Sb Doped ZnO NPs

The synthesis process is similar to that of Sn doped ZnO *NPs*; only $AlCl_3$ (0.5 mol%, 1 mol%, and 5 mol%) or $SbCl_3$ (0.5 mol%, 1 mol%, and 5 mol%) were used to replace $SnCl_4{\cdot}5H_2O$. Those samples were defined as Al0.5-ZnO, Al1-ZnO, Al5-ZnO, Sb0.5-ZnO, Sb1-ZnO, and Sb5-ZnO, respectively.

2.3. Characterization

X-ray diffraction (XRD) was carried out to investigate the crystallographic structures using Cu Kα radiation (λ = 0.15418 nm) with an X-ray diffractometer (Rigaku D/Max–2550). Field emission scanning electron microscopy (FESEM, XL 30 ESEM FEG) and transmission electron microscopy (TEM, JEOL JEM–2100F) were applied to survey the morphologies of the ZnO NPs. The samples were qualitatively studied by an X-ray photoelectron spectrometer (XPS, ESCALAB MK II). A CGS-8 test instrument (China, ELITE TECH) was used to estimate the resistance of the gas sensors.

2.4. Measurement of Gas Sensors

The powders were dispersed in a specified amount of ethanol, and then ground for 15 min. ZnO NPs have different doping concentrations, as sensitive materials are uniformly layered on alumina ceramic tubes [22]. After that, the nickel–chromium alloy coil is inserted into the ceramic tube in order to control the operating temperature (Figure S1, Supplementary Material). The gas sensors were aged at 280 °C for 24 h to obtain stable gas

sensors. A simple test system was applied to survey the gas-sensing properties (Figure S1b). Using the static liquid gas distribution method, acetone was injected into the test chamber (1 L) through a micro syringe, during the gas test. The required gas concentration is calculated according to the formula:

$$c = \frac{22.4 \times \beta \times \rho \times 10^9 \times V_1}{M \times V_2}$$

For the formula, c (ppm) is the gas concentration; β (g/mL) is the density of the liquid; ρ is the purity of the liquid; V_1 (L) and V_2 (L) are the volume of the liquid and the test chamber, respectively; and M (g/mol) is the molecular weight of the gas. For gases such as ammonia, this formula can match the reaction process of preparing NH_3 from an ammonia solution ($NH_3 \cdot H_2O$, 25%–28%). The quantitative solution was then extracted and injected into the test chamber. The powders were dispersed in a specified amount of ethanol. The response was determined by the resistance ratio (R_a/R_g). Note that R_a is original resistance in dry air atmosphere, and R_g is the resistance in target gas atmosphere. The response/recovery time is defined by measuring the time that the resistance changes from the initial value to 90% of the total resistance variation after the sensor is exposed to the test gas (adsorption) and pure air (desorption), respectively.

3. Results

3.1. Material Synthesis and Structural Characterization

As shown in Figure S2, the XRD analysis confirmed that the pure ZnO samples possess a well-crystallized wurtzite structure (JCPDS card no. 99-0111). All materials were tested and compared with the XRD results of pure ZnO. The diffractions from the (1 0 0), (0 0 2), (1 0 1), (1 0 2), (1 1 0), and (1 0 3) lattice planes of doped ZnO samples are similar to those of pure ZnO, indicating that no additional phase is detected (Figure 1a–c) [11–13]. The average crystallite size (D) of ZnO doped with different cations is estimated by the Scherrer formula, using (101) facets:

$$D = \frac{0.9\lambda}{\beta \cos\theta}$$

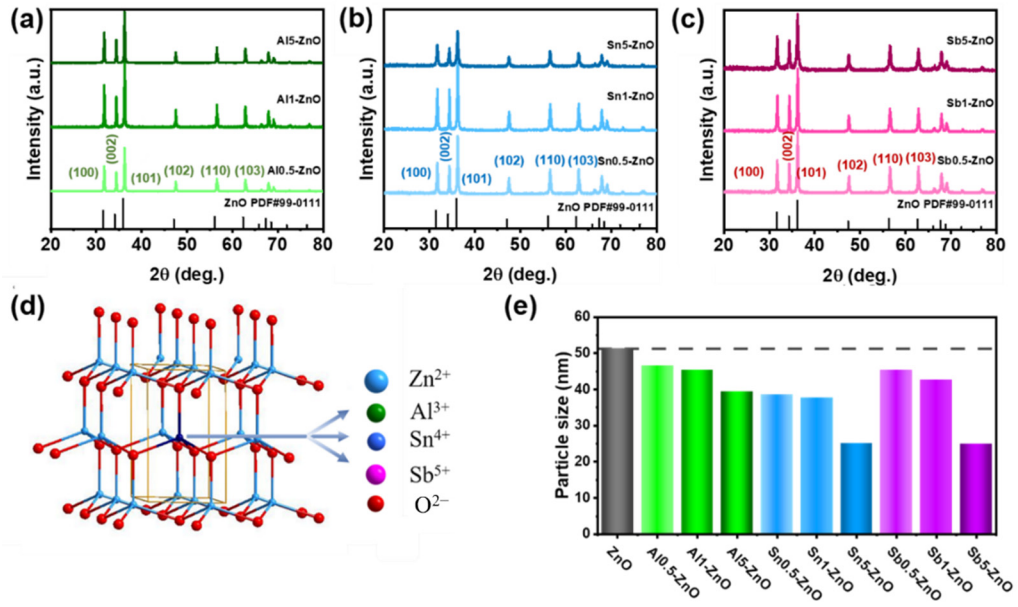

Figure 1. (**a**–**c**) XRD patterns of various samples. (**d**) The ball and stick model of ZnO crystal structure for which the Zn^{2+} is replaced by Al^{3+}, Sn^{4+}, or Sb^{5+}. (**e**) Average crystallite size of ZnO and various dopants doped ZnO.

Among these, λ and β are the wavelengths of Cu Kα radiation and the strongest peak of FWHM, respectively [23]. Because of the much smaller ionic radius of Al^{3+} (53.5 pm), Sn^{4+} (69 pm), and Sb^{5+} (60 pm) compared with Zn^{2+} (74 pm), the dopants are easily incorporated into the ZnO lattice (Figure 1d) [17,24]. In addition, as the doping ratio increases from 0.5 mol% to 5 mol%, the calculated D continuously decreases (Figure 1e), which means that the dopants effectively inhibit the grain growth of ZnO crystallites.

The FESEM image for the pure ZnO NPs is illustrated in Figure 2a, which shows that ZnO NPs have a rod-shaped structure with length in the range of 700–800 nm. Figure 2b–d show the structure and morphology of the prepared Al0.5-ZnO, Sn0.5-ZnO, and Sb0.5-ZnO samples, respectively. By doping different metallic cations into ZnO, the size of those NPs is obviously reduced. Figure 2b shows that Al0.5-ZnO has a similar rod structure. The length of Al0.5-ZnO nanorods is mainly concentrated at 130 nm, which is much shorter than that of pure ZnO. From the FESEM image of Figure 2c, it is obvious that Sn0.5-ZnO materials are consisted of irregular particles with the diameter of ca. 110 nm, indicating that introducing Sn^{4+} cations inhibits the growth of ZnO. For Sb0.5-ZnO materials, the rod structure is missing from the FESEM view, and a mass of non-uniform block-shaped particles was formed (Figure 2d).

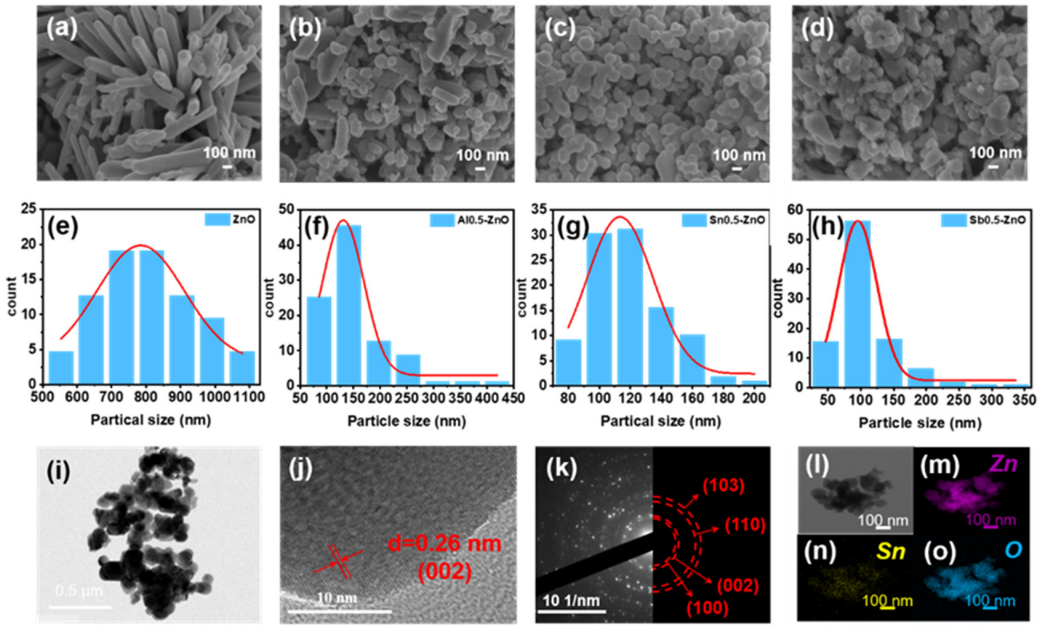

Figure 2. (**a**–**d**) FESEM images of ZnO, Al0.5-ZnO, Sn0.5-ZnO, and Sb0.5-ZnO, respectively. (**e**–**h**) particle size count images of ZnO, Al0.5-ZnO, Sn0.5-ZnO, and Sb0.5-ZnO, respectively. (**i**) TEM, (**j**) HRTEM images, (**k**) SAED pattern, and (**l**–**o**) EDX mapping of the Sn0.5-ZnO.

The morphology of Sn0.5-ZnO was further surveyed with TEM (Figures 2 and S3). The structure of Sn0.5-ZnO materials from Figure 2i shows no difference with the SEM results. By further characterization, the HRTEM photograph (Figure 2j) demonstrates that the lattice fringe spacing is ca. 0.26 nm, which coincides with the (002) crystal plane of ZnO samples. Selected area electron diffraction (SAED) patterns of the samples are matched with the crystal planes of (002), (100), (110), and (103), respectively [25]. Moreover, a uniform distribution of Zn, Sn, and O elements into the materials was verified in Figure 2l–o. The EDS elemental mapping images also demonstrate that Sn cations are successfully doped into the ZnO matrix.

In order to investigate the elemental composition and chemical valence, XPS was performed as shown in Figures 3 and S4. Figure 3a–c show the Al 2s, Sn 3d, and Sb 3d XPS spectra of Al0.5-ZnO, Sn0.5-ZnO, and Sb0.5-ZnO, respectively. The Al 2s spectrum revealed a peak at around 119.36 eV, which indicates the existence of Al in the ZnO materials.

Although the intensity of the peak of Al 2s is relatively low, the peaks of Zn $2p_{1/2}$ and Zn $2p_{3/2}$ shift towards higher binding energy, which indicates that the Al is incorporated into the Zn^{2+} sites of ZnO (Figure S5) [11,26]. Figure 3b shows the Sn 3d spectrum, which has three obvious peaks. The peaks at 486.1 eV and 494.5 eV could be nominated to Sn $3d_{5/2}$ and Sn $3d_{3/2}$, respectively. The calculated spin–orbit splitting value (8.4 eV) agrees with the standard XPS spectrum, proving that Sn was in the Sn^{4+} oxidation state, as well as the success of Sn doping. The peak at 497.7 eV is assigned to Zn LM2 Auger [27,28]. Figure 3c shows the peaks of Sb 3d, which has two different peaks at 531.5 eV and 540.4 eV [20,29,30]. Figure 3d–g show the O 1s XPS spectra, which are separated into chemisorbed oxygen species (O_C), oxygen vacancy (O_V), and lattice oxygen species (O_L) [31]. There is the highest relative proportion of O_C for Sn0.5-ZnO in Table 1 after calculating the XPS results, suggesting that introducing Sn^{4+} can enhance the oxygen chemisorbed ability of ZnO NPs.

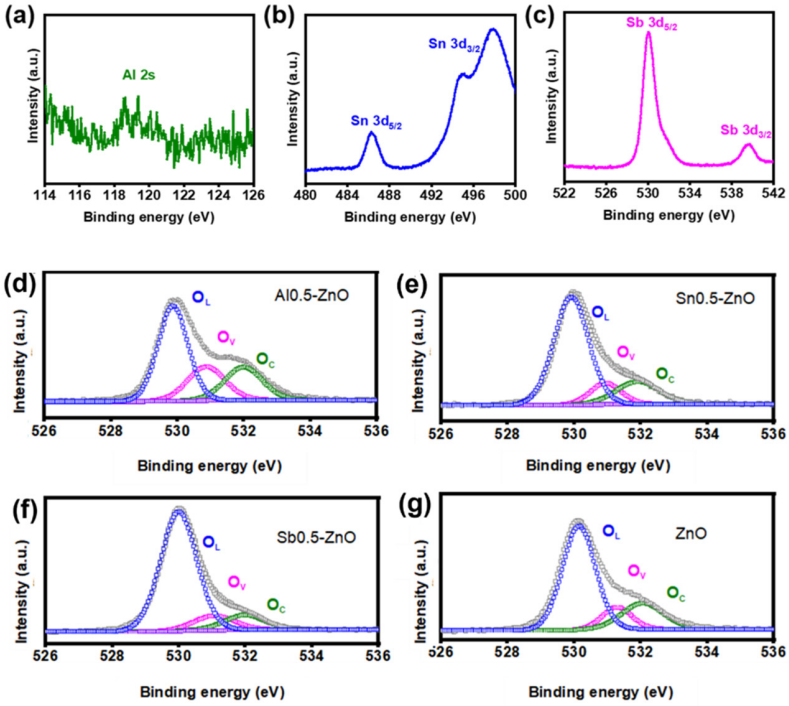

Figure 3. XPS spectra: (**a**) Al 2s of Al0.5-ZnO, (**b**) Sn 3d of Sn0.5-ZnO, and (**c**) Sb 3d of Sb0.5-ZnO. O 1s of (**d**) Al0.5-ZnO, (**e**) Sn0.5-ZnO, (**f**) Sb0.5-ZnO, and (**g**) ZnO.

Table 1. Comparison of resistance values of different sensors.

Sensitive Materials	Preparation Method	Original Resistance (MΩ)	Reference
Ga-doped ZnO nanofibers functionalized with Pt catalysts	Electrospinning	93.2	[16]
ZnO@In_2O_3@ZnO hollow microspheres	Oil bath hydrothermal reaction	120	[10]
Pt@Al-doped ZnO core–shell nanoparticles	Hydrothermal reaction	17,000	[11]
ZnO nano-particle thin films	Sol-gel	110	[23]
Positive Ion doped ZnO nanoparticle	Sol-gel	0.28	This work

3.2. Measurement of Gas Sensors

Figure 4a–c show the original resistance change of gas sensors-based ZnO NPs before and after doping Al^{3+}, Sn^{4+} and Sb^{5+} ions in the temperature range of 250–300 °C by using logarithmic axes. The original resistance of the sensors decreases with the working

temperature increasing. In Figure 4a, the resistances of Al0.5-ZnO and Al1-ZnO are much lower that of the pure ZnO NPs. However, when the doping concentration reaches 5 mol%, the resistance of Al5-ZnO is almost twice as high as that of the pure ZnO NPs. This is because of the poor stability of the Al element and the formation of a small amount of alumina as the doping concentration increases [32]. The resistance of Sn^{4+} doped ZnO based gas sensors was illustrated in Figure 4b. The resistances of Sn0.5-ZnO and Sn1-ZnO were also lower than those of ZnO NPs. For Sn5-ZnO, the resistances are lower from 250 to 270 °C, and similar with pure ZnO NPs when the temperature is above 280 °C. Figure 4c shows that the resistance of three samples (Sb0.5-ZnO, Sb1-ZnO, and Sb5-ZnO) is substantially lower than pure ZnO NPs [33]. For the purpose of comparing the influence of various dopants on the original resistance of the gas sensors, the resistance change value ($\Delta R = RS - RZnO$) of different samples (R_S) compared with the pure ZnO (R_{ZnO}) is defined. Herein, the temperature for gas sensors is restricted to 270 °C, as shown in Figure 4d–f. Among all the samples with the same cation-doping concentration, ΔR values for Sn-doped ZnO and Sb-doped ZnO are larger than that of Al-doped ZnO. The original resistances reduced by 4.63, 4.91, and 4.92 MΩ for Al0.5-ZnO, Sn0.5-ZnO, and Sb0.5-ZnO, respectively. In Table 1, the resistance value of the sensor based on Sn0.5-ZnO is compared with that of other sensors, highlighting the advantage of the sensor resistance value obtained in this work.

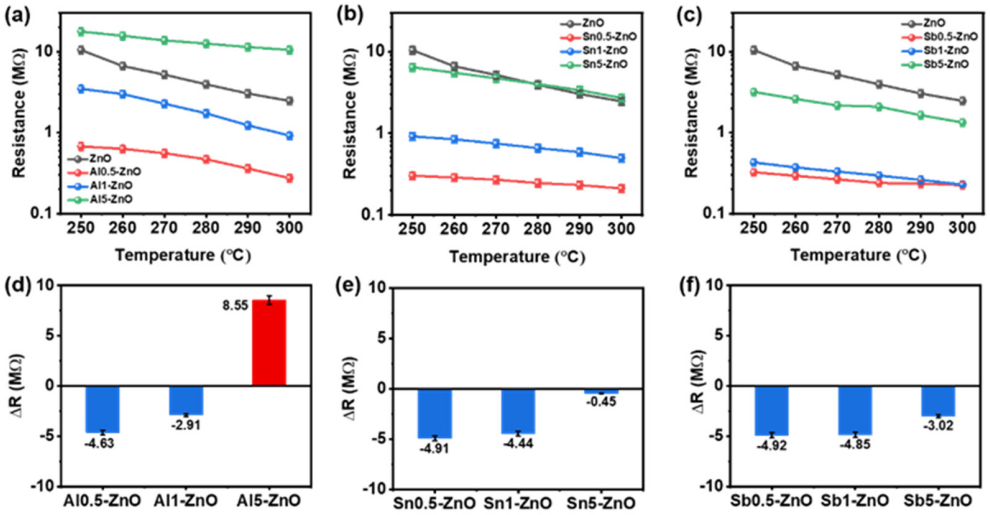

Figure 4. (**a**–**c**) The baseline resistance of ZnO and various dopants doped ZnO at different temperatures (250–300 °C). (**d**–**f**) ΔR = RS − RZnO (R_S is indicated as the resistances of Al0.5-ZnO, Al1-ZnO, Al5-ZnO, Sn0.5-ZnO, Sn1-ZnO, Sn5-ZnO, Sb0.5-ZnO, Sb1-ZnO, and Sb5-ZnO, respectively) at 270 °C.

The working temperature is one of the key factors affecting gas sensing performances. Based on the lower original resistance, the optimal operating temperatures for gas sensors based on Al0.5-ZnO, Sn0.5-ZnO, and Sb0.5-ZnO were measured as shown in Figure 5a. After doping with 0.5 mol% of Al, Sn, and Sb, the optimal operating temperature is 270 °C when the sensors are exposed to 100 ppm of acetone. With the temperature rising from 250 °C to the optimal operating temperature (270 °C), the response is improved due to introducing more reactive oxygen species to react with acetone. However, a temperature higher than the optimum working temperature will lead to a rapid desorption rate of acetone molecules, thereby reducing the response of the gas sensors [34]. It is worth noting that the responses of sensors based on ZnO NPs and Sn0.5-ZnO NPs to 100 ppm acetone are significantly higher than those of Al0.5-ZnO and Sb0.5-ZnO NPs. The highest responses for sensors based on ZnO and Sn0.5-ZnO NPs are 10.99 and 10.95, respectively. This suggests that the sensors based on Sn0.5-ZnO NPs obtained a higher response to acetone as well as a lower original resistance. Next, a series of response tests of different concentrations of acetone were carried out on sensors based on Al0.5-ZnO, Sn0.5-ZnO, and Sb0.5-ZnO

(Figure 5b). The results show that the sensor based on Sn0.5-ZnO showed the highest acetone responses. Thus, the Sn0.5-ZnO sensor was used for further investigation of gas sensing performances.

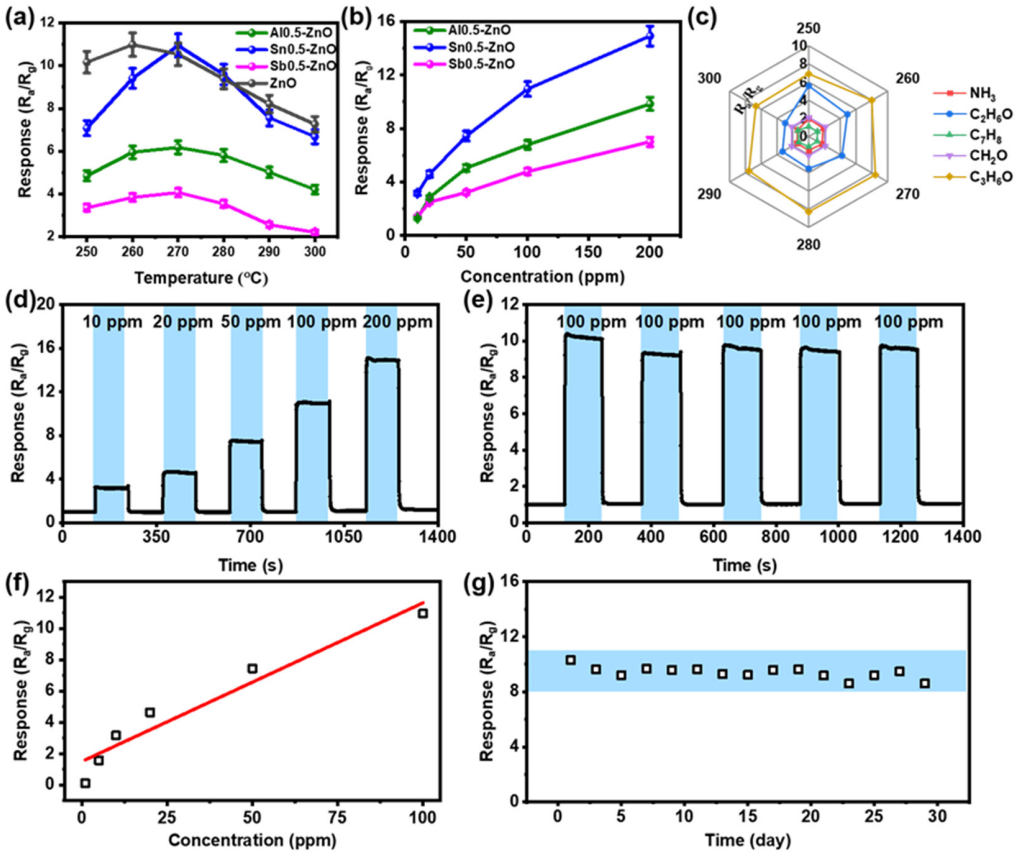

Figure 5. (**a**) The responses to 100 ppm acetone of various elements of doped M0.5-ZnO and ZnO samples at different temperatures (250–300 °C). (**b**) The response of 0.5 mol% Al^{3+}, Sn^{4+} and Sb^{5+} doped ZnO to different concentrations of acetone (10–200 ppm). (**c**) The response of the Sn0.5-ZnO to 100 ppm NH_3, C_2H_6O, C_7H_8, CH_2O, and C_3H_6O at different temperatures (250–300 °C), respectively. (**d**) The response of the Sn0.5-ZnO to 10–200 ppm acetone at 270 °C. (**e**) Five cycles of the response/recovery curve of the Sn0.5-ZnO sensor to 100 ppm acetone at 270 °C. (**f**) Linear fitting curve for the response of the Sn0.5-ZnO to 1–100 ppm acetone at 270 °C. (**g**) Long-term stability of the Sn0.5-ZnO after 30 days.

Figure 5c shows the responses to gases including NH_3, C_2H_6O, C_7H_8, CH_2O, and C_3H_6O (100 ppm) for sensors based on Sn0.5-ZnO. The sensor obtained the highest response to acetone from 250 to 300 °C, indicating great selectivity. The Sn0.5-ZnO-based sensor also exhibited a fast response time (1 s) and recovery time (10 s) to acetone (Figure S6). Figure 5d shows the responses to 10–200 ppm of acetone at 270 °C. The responses to 10, 20, 50, 100, and 200 ppm of acetone are 3.16, 4.61, 7.64, 10.95, and 14.91, respectively. The limit of detection is as low as 1 ppm, as shown in Figure 5f. Finally, the gas sensor based on Sn0.5-ZnO was cyclically tested to 100 ppm acetone. The responses and the resistance are reproducible during five-cycle sensing measurement, as shown in Figures 5e and S7. The response value remained basically stable within 30 days, which shows that Sn0.5-ZnO sensors have great long-term stability.

3.3. Gas Sensing Mechanism

In this paper, the influence of doping on the material resistance is explained by the following two aspects: (1) The resistance of Sn and Sb doped ZnO is lower than that of Al doped ZnO. The doping of cations in the lattice can be expressed as electron compensation,

that is, the generation of electrons and oxygen gas, as shown in Equations (2)–(4). Under the same doping concentration, Sn^{4+} and Sb^{5+} have a higher oxidation state than Al^{3+} (as evidenced by XPS results) to provide more free electrons when doped into ZnO NPs (Equations (2)–(4)). Thus, the effective electron compensation effect of Sn and Sb with higher valence states results in relatively low original resistances. (2) The resistance gradually increases with the doping concentration, increasing from 0.5 mol% to 5 mol% for the Al/Sn/Sb-doped ZnO. In the case of high doping concentration, the doped cations are easy to enter the interstitial position [32]. Interstitial ionic impurities act as electron scattering centers to reduce carrier mobility and increase the resistances.

Moreover, the Burstein–Moss effect shows that more energy is required for electrons to excite from the valence band to the conduction band of doped semiconductors. This is due to the introduction of free electrons by doping, which leads to the collection of electrons in the conduction band [12,29].

$$\frac{1}{2}Al_2O_3 \overset{ZnO}{\rightarrow} Al_{Zn}^{\cdot} + e' + O_O^X + O_2(g)$$

$$SnO_2 \overset{ZnO}{\rightarrow} Sn_{Zn}^{\cdot\cdot} + 2e' + O_O^X + \frac{1}{2}O_2(g)$$

$$\frac{1}{2}Sb_2O_5 \overset{ZnO}{\rightarrow} Sb_{Zn}^{\cdots} + 3e' + O_O^X + \frac{3}{4}O_2(g)$$

The widely accepted gas sensing mechanism, based on ZnO semiconductors-based gas sensors, depends on the modulation of the thickness of the surface electron depletion layer, which is caused by electron transfer between target gas molecules and chemisorbed oxygen [35]. As shown in Figure 6, for the n-type ZnO semiconductor, the surface of the ZnO material chemically adsorbs oxygen to obtain electrons from the conduction band, which leads to a raise in terms of material resistance. The reducing acetone gas would react with chemically adsorbed oxygen to release electrons during the gas-sensing reaction; this causes the resistance of the semiconductor to decrease. The reaction equation is as follows:

$$H_3COCH_3(g) + 8O^- \rightarrow 3CO_2 + 3H_2O + 8e^-$$

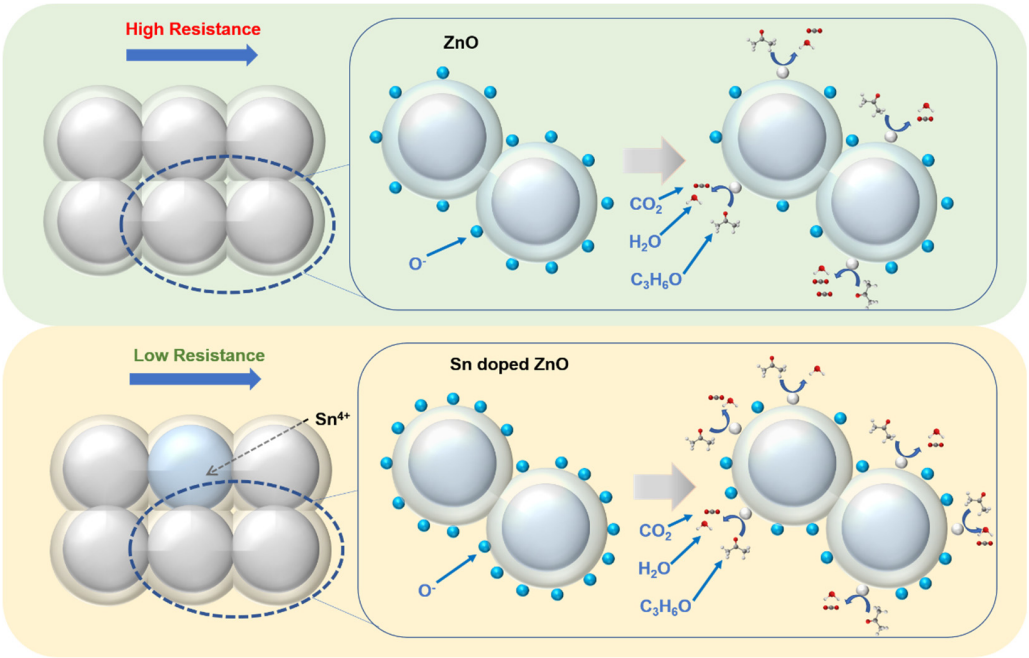

Figure 6. Schematic diagram of the acetone gas sensing mechanism.

Compared with undoped ZnO, the doping of higher valence Sn^{4+} into ZnO will increase the concentration of electrons, leading to a relatively low resistance. Meanwhile, the concentration of chemically adsorbed oxygen on the exterior of the Sn-doped ZnO materials is also improved. The O_c concentrations in Al0.5-ZnO, Sn0.5-ZnO, and Sb0.5-ZnO are 20.4%, 22.3%, and 11.3%, respectively (Table 2).

Table 2. Fitting results of O 1s XPS spectra of ZnO NPs and different cations (Al^{3+}, Sn^{4+}, and Sb^{5+}) doped ZnO NPs.

Sample	Oxygen Species	Binging Energy (eV)	Percentage
Al0.5-ZnO	OL	529.87	61.2%
	OV	530.87	18.4%
	OC	531.99	20.4%
Sn0.5-ZnO	OL	529.90	67.5%
	OV	530.94	10.2%
	OC	531.90	22.3%
Sb0.5-ZnO	OL	529.99	78.6%
	OV	531.05	10.1%
	OC	531.98	11.3%
ZnO	O_L	530.13	68%
	O_V	531.23	10.2%
	O_C	532.08	21.1%

Based on XPS spectral analysis, 0.5 mol% Sn doped ZnO NPs has the highest chemisorption oxygen concentration compared to Al and Sb doped samples. The doping of Sn^{4+} makes it easier for ZnO to obtain active sites for adsorbing oxygen. The increased O_c will react with the acetone to generate more free electrons, thereby significantly enhancing the responses for the gas sensors [36]. By calculating the XPS results, it can be concluded that the O_C ratio of ZnO is higher than that of Al0.5-ZnO and Sb0.5-ZnO, but it is lower than that of Sn0.5-ZnO, which is consistent with the results of the gas sensing test. Therefore, ZnO with Sn doping can achieve the goal of reducing original resistance and obtaining a great response.

4. Conclusions

In this work, pure ZnO NPs and ZnO NPs doped with different cations (Al^{3+}, Sn^{4+}, and Sb^{5+}) were synthesized. Meanwhile, the acetone sensing performances were surveyed. Conclusions show that the sensors based on Sn0.5-ZnO exhibit the best performance in detecting 100 ppm of C_3H_6O with the high response of 10.54 and relatively low basic resistance (0.28 MΩ). By introducing Sn^{4+} into ZnO nanoparticles (NPs), the resistance was significantly reduced without sacrificing gas sensitivity. This is due to the synergistic effects of electron compensation and improved adsorbing oxygen ability. Therefore, we have successfully prepared a low-resistance gas sensor that is able to achieve our expected goal, and that has a good application prospect.

Supplementary Materials: The following supporting information can be downloaded at: https://www.mdpi.com/article/10.3390/chemosensors10090364/s1, Figure S1: Schematic diagram of (**a**) the sensor structure and (**b**) sensing measurement process using CGS–8 Intelligent Test Meter, Figure S2: XRD spectrum of ZnO NPs prepared by the sol-gel method, Figure S3: HRTEM and TEM images of Sn0.5-ZnO, Figure S4: XPS survey spectra of Al0.5-ZnO, Sn0.5-ZnO and Sb0.5-ZnO, Figure S5: Zn 2p XPS survey spectra of Al0.5-ZnO and ZnO, Figure S6: The response and recover curve of sensors based on Sn0.5-ZnO to 100 ppm acetone at 270 °C, Figure S7: The resistance change of sensors based on Sn0.5-ZnO when the sensor was exposed to 100 ppm acetone.

Author Contributions: Conceptualization, T.Z. (Tong Zhang); methodology, T.Z. (Tingting Zhou); investigation, S.C. and Y.X.; resources, N.S. and Y.H.; writing—original draft preparation, P.Z.; writing—review and editing, T.Z. (Tingting Zhou); All authors have read and agreed to the published version of the manuscript.

Funding: This work was supported by the Natural Science Foundation Committee (NSFC, Grant No. 62020106006 and No. 62101208), the China Postdoctoral Science Foundation (2021M691196).

Data Availability Statement: The data presented in this study are available on request from the corresponding author.

Conflicts of Interest: The authors declare no conflict of interest.

References

1. Zhou, T.T.; Zhang, T. Recent progress of nanostructured sensing materials from 0D to 3D: Overview of structure–property-application relationship for gas sensors. *Small Methods* **2021**, *5*, 2100515. [CrossRef] [PubMed]
2. Liu, X.H.; Ma, T.T.; Pinna, N.; Zhang, J. Two-dimensional nanostructured materials for gas sensing. *Adv. Funct. Mater.* **2017**, *27*, 1702168. [CrossRef]
3. Ghule, B.G.; Shinde, N.M.; Raut, S.D.; Shaikh, S.F.; Al-Enizi, A.M.; Kim, K.H.; Mane, R.S. Porous metal-graphene oxide nanocomposite sensors with high ammonia detectability. *J. Colloid Interface Sci.* **2021**, *589*, 401–410. [CrossRef] [PubMed]
4. Yang, F.; Guo, Z. Engineering NiO sensitive materials and its ultra-selective detection of benzaldehyde. *J. Colloid Interface Sci.* **2016**, *467*, 192–202. [CrossRef] [PubMed]
5. Yuan, K.P.; Zhu, L.Y.; Yang, J.H.; Hang, C.Z.; Tao, J.J.; Ma, H.P.; Jiang, A.Q.; Zhang, D.W.; Lu, H.L. Precise preparation of WO_3@SnO_2 core shell nanosheets for efficient NH_3 gas sensing. *J. Colloid Interface Sci.* **2020**, *568*, 81–88. [CrossRef] [PubMed]
6. Nguyen, T.T.D.; van Dao, D.; Kim, D.S.; Lee, H.J.; Oh, S.Y.; Lee, I.H.; Yu, Y.T. Effect of core and surface area toward hydrogen gas sensing performance using Pd@ZnO core-shell nanoparticles. *J. Colloid Interface Sci.* **2021**, *587*, 252–259. [CrossRef]
7. Sui, N.; Cao, S.; Zhang, P.; Zhou, T.; Zhang, T. The effect of different crystalline phases of In_2O_3 on the ozone sensing performance. *J. Hazard. Mater.* **2021**, *418*, 126290. [CrossRef]
8. Miller, D.R.; Akbar, S.A.; Morris, P.A. Nanoscale metal oxide-based heterojunctions for gas sensing: A review. *Sens. Actuators B Chem.* **2014**, *204*, 250–272. [CrossRef]
9. Li, L.; Zhang, C.; Chen, W. Fabrication of SnO_2-SnO nanocomposites with p-n heterojunctions for the low-temperature sensing of NO_2 gas. *Nanoscale* **2015**, *7*, 12133–12142. [CrossRef]
10. Wang, S.; Wang, X.; Qiao, G.; Chen, X.; Wang, X.; Cui, H. Core-double shell ZnO@In_2O_3@ZnO hollow microspheres for superior ethanol gas sensing. *Sens. Actuators B Chem.* **2021**, *341*, 130002. [CrossRef]
11. Gong, Y.; Wu, X.; Li, X.; Wang, A.; Zhang, M.; Chen, Y. Enhanced acetone sensing properties of Pt@Al-doped ZnO core-shell nanoparticles. *Sens. Actuators B Chem.* **2021**, *329*, 129153. [CrossRef]
12. Shewale, P.S.; Yu, Y.S.; Kim, J.H.; Bobade, C.R.; Uplane, M.D. H_2S gas sensitive Sn-doped ZnO thin films: Synthesis and characterization. *J. Anal. Appl. Pyrolysis* **2015**, *112*, 348–356. [CrossRef]
13. Hsu, C.L.; Chen, K.C.; Tsai, T.Y.; Hsueh, T.J. Fabrication of gas sensor based on p-type ZnO nanoparticles and n-type ZnO nanowires. *Sens. Actuators B Chem.* **2013**, *182*, 190–196. [CrossRef]
14. Li, J.; Xian, J.; Wang, W.; Cheng, K.; Zeng, M.; Zhang, A.; Wu, S.; Gao, X.; Lu, X.; Liu, J.M. Ultrafast response and high-sensitivity acetone gas sensor based on porous hollow Ru-doped SnO_2 nanotubes. *Sens. Actuators B Chem.* **2022**, *352*, 131061. [CrossRef]
15. Shen, Y.; Yamazaki, T.; Liu, Z.; Meng, D.; Kikuta, T.; Nakatani, N.; Saito, M.; Mori, M. Microstructure and H_2 gas sensing properties of undoped and Pd-doped SnO_2 nanowires. *Sens. Actuators B Chem.* **2009**, *135*, 524–529. [CrossRef]
16. Park, S.; Bulemo, P.M.; Koo, W.T.; Ko, J.; Kim, I.D. Chemiresistive acetylene sensor fabricated from Ga-doped ZnO nanofibers functionalized with Pt catalysts. *Sens. Actuators B Chem.* **2021**, *343*, 130137. [CrossRef]
17. Ebrahimifard, R.; Golobostanfard, M.R.; Abdizadeh, H. Sol-gel derived Al and Ga co-doped ZnO thin films: An optoelectronic study. *Appl. Surf. Sci.* **2014**, *290*, 252–259. [CrossRef]
18. Han, N.; Chai, L.; Wang, Q.; Tian, Y.; Deng, P.; Chen, Y. Evaluating the doping effect of Fe, Ti and Sn on gas sensing property of ZnO. *Sens. Actuators B Chem.* **2010**, *147*, 525–530. [CrossRef]
19. Chen, H.D.; Jin, K.L.; Xu, J.C.; Han, Y.B.; Jin, H.X.; Jin, D.F.; Peng, X.L.; Hong, B.; Li, J.; Yang, Y.T.; et al. High-valence cations-doped mesoporous nickel oxides nanowires: Nanocasting synthesis, microstructures and improved gas-sensing performance. *Sens. Actuators B Chem.* **2019**, *296*, 126622. [CrossRef]
20. Kim, J.H.; Mirzaei, A.; Kim, J.Y.; Lee, J.H.; Kim, H.W.; Hishita, S.; Kim, S.S. Enhancement of gas sensing by implantation of Sb-ions in SnO_2 nanowires. *Sens. Actuators B Chem.* **2020**, *304*, 127307. [CrossRef]
21. Han, N.; Wu, X.; Zhang, D.; Shen, G.; Liu, H.; Chen, Y. CdO activated Sn-doped ZnO for highly sensitive, selective and stable formaldehyde sensor. *Sens. Actuators B Chem.* **2011**, *152*, 324–329. [CrossRef]
22. Zhou, T.T.; Cao, S.; Zhang, R.; Tu, J.; Fei, T.; Zhang, T. Effect of Cation Substitution on the Gas-Sensing Performances of Ternary Spinel MCo_2O_4 (M = Mn, Ni, and Zn) Multishelled Hollow Twin Spheres. *ACS Appl. Mater. Interfaces* **2019**, *11*, 28023–28032. [CrossRef] [PubMed]
23. Trinh, T.T.; Tu, N.H.; Le, H.H.; Ryu, K.Y.; Le, K.B.; Pillai, K.; Yi, J. Improving the ethanol sensing of ZnO nano-particle thin films—The correlation between the grain size and the sensing mechanism. *Sens. Actuators B Chem.* **2011**, *152*, 73–81. [CrossRef]
24. Lupan, C.; Khaledialidusti, R.; Mishra, A.K.; Postica, V.; Terasa, M.I.; Magariu, N.; Pauporté, T.; Viana, B.; Drewes, J.; Vahl, A.; et al. Pd-functionalized ZnO: Eu columnar films for room-temperature hydrogen gas sensing: A combined experimental and computational approach. *ACS Appl. Mater. Interfaces* **2020**, *12*, 24951–24964. [CrossRef]

25. Li, Z.; Zhang, Y.; Zhang, H.; Jiang, Y.; Yi, J. Superior NO_2 sensing of MOF-derived indium-doped ZnO porous hollow cages. *ACS Appl. Mater. Interfaces* **2020**, *12*, 37489–37498. [CrossRef]
26. Yoo, R.; Güntner, A.T.; Parka, Y.; Rim, H.J.; Lee, H.-S.; Lee, W. Sensing of acetone by Al-doped ZnO. *Sens. Actuators B Chem.* **2019**, *283*, 107–115. [CrossRef]
27. Yao, M.; Ding, F.; Cao, Y.; Hu, P.; Fan, J.; Lu, C.; Yuan, F.; Shi, C.; Chen, Y. Sn doped ZnO layered porous nanocrystals with hierar chical structures and modified surfaces for gas sensors. *Sens. Actuators B Chem.* **2014**, *201*, 255–265. [CrossRef]
28. Zhao, S.; Shen, Y.; Maboudian, R.; Carraro, C.; Han, C.; Liu, W.; Wei, D. Facile synthesis of ZnO-SnO_2 hetero-structured nanowires for high-performance NO_2 sensing application. *Sens. Actuators B Chem.* **2021**, *333*, 129613. [CrossRef]
29. Liu, X.; Tian, X.; Jiang, X.; Jiang, L.; Hou, P.; Zhang, S.; Sun, X.; Yang, H.; Cao, R.; Xu, X. Facile preparation of hierarchical Sb-doped In_2O_3 microstructures for acetone detection. *Sens. Actuators B Chem.* **2018**, *270*, 304–311. [CrossRef]
30. Ma, J.; Liu, Y.; Zhang, H.; Ai, P.; Gong, N.; Wu, Y.; Yu, D. Room temperature ppb level H_2S detection of a single Sb-doped SnO_2 nanoribbon device. *Sens. Actuators B Chem.* **2015**, *216*, 72–79. [CrossRef]
31. Zhang, Y.; Liu, Y.; Zhou, L.; Liu, D.; Liu, F.; Liu, F.; Liang, X.; Yan, X.; Gao, Y.; Lu, G. The role of Ce doping in enhancing sensing performance of ZnO-based gas sensor by adjusting the proportion of oxygen species. *Sens. Actuators B Chem.* **2018**, *273*, 991–998. [CrossRef]
32. Hagedorn, K.; Li, W.; Liang, Q.; Dilger, S.; Noebels, M.; Wagner, M.R.; Reparaz, J.S.; Dollinger, A.; der Günne, J.S.A.; Dekorsy, T.; et al. Catalytically doped semiconductors for chemical gas sensing: Aerogel-like aluminum-containing zinc oxide materials prepared in the gas phase. *Adv. Funct. Mater.* **2016**, *26*, 3424–3437. [CrossRef]
33. Chaparadza, A.; Rananavare, S.B. Room temperature Cl_2 sensing using thick nanoporous films of Sb-doped SnO_2. *Nanotechnology* **2008**, *19*, 245501. [CrossRef] [PubMed]
34. Xing, L.L.; Yuan, S.; Chen, Z.H.; Chen, Y.J.; Xue, X.Y. Enhanced gas sensing performance of SnO_2/α-MoO_3 heterostructure nanobelts. *Nanotechnology* **2011**, *22*, 225502. [CrossRef] [PubMed]
35. Zhou, T.T.; Zhang, R.; Wang, Y.; Zhang, T. MOF–derived 1 D A–Fe_2O_3/$NiFe_2O_4$ heterojunction as efficient sensing materials of acetone vapors. *Sens. Actuators B Chem.* **2019**, *281*, 885–892. [CrossRef]
36. Jiang, F.X.; Tong, R.X.; Yan, Z.; Ji, L.F.; Xu, X.H. *d*-electron-dependent transparent conducting oxide of V-doped ZnO thin films. *J. Alloy. Compd.* **2020**, *822*, 153706. [CrossRef]